Characteristic Landslide Distributions: An Investigation of Landscape Controls on Landslide Size (*Published in EPSL*, *April 2020*)

William G. Medwedeff^{1*}, Marin K. Clark¹, Dimitrios Zekkos²†, A. Joshua West³

† Now at Department of Civil and Environmental Engineering, Univ. of California at Berkeley, 733 Davis Hall, Berkeley, CA 94720

Abstract

Estimation of landslide erosion rates and hazard prediction require a firm understanding of the physical controls on landslide size. In this study we seek to understand how the characteristics of different landscapes and forcing events influence the distribution of landslide size at a regional scale. We explore the parameter space of a mechanically-based landslide model through a series of simulations using digital elevation data. Consistent with previous studies, we find that large slope failures are infrequent due to the scarcity of large, steep hillslopes in typical mountainous topography. On the other hand, we find that the occurrence of small landslides is limited by the cohesive strength of hillslope material, which overcomes the weaker driving forces on short slopes. We test our model results with an empirical investigation of frequency-size distributions for eight real co-seismic landslide inventories. Although empirical data are noisy, we find a positive correlation between landslide size and hillslope relief, while the effects of PGA on landslide size are less pronounced. We conclude that landslide size distributions reflect the available distribution of hillslope geometries in a given landscape, and that external forcing (e.g., seismic ground motion) determines which subset of the hillslope distribution fails during a particular event. For a given landscape and forcing event, there is a particular length-scale over which landsliding is statistically favored, leading to the concept of characteristic landslide size distributions.

Keywords: landslides; earthquakes; power-law; frequency size scaling; hillslope relief; lognormal; scale invariant

1 Introduction

Landslide size is a strong predictor of the runout distance for a variety of different landslide types (Legros, 2002; Roback et al., 2018) and is an important factor to consider in hazard prediction. Runout distance controls the connectivity of landslide debris with the fluvial system (Li et al., 2016; Roback et al., 2018), thus dictating the degree to which landslides contribute to secondary hazards such as flooding and debris flows (Fan et al., 2019) as well as influencing how landslides contribute to the erosion budget of mountain belts (Li et al., 2014). While prediction of landslide size is routine in geotechnical investigations, robust estimation of the critical failure surface requires site-specific measurements of subsurface material properties and slope geometries, which

¹ Department of Earth and Environmental. Sciences, Univ. of Michigan, 1100 North University Ave., Ann Arbor, MI 48109

² Department of Civil and Environmental Engineering, Univ. of Michigan, 2350 Hayward Str., Ann Arbor, MI 48109

³ Department of Earth Sciences, University of Southern California, 3651 Trousdale Parkway, Los Angeles, CA 90089

^{*} Corresponding author: wmedwed@umich.edu

are impractical to collect at regional scales. In place of such detailed investigation, landslide inventories mapped after large rainstorms or earthquakes provide the opportunity to statistically investigate the physical controls on landslide size. The growing availability of earthquake triggered inventories in particular has facilitated recent comparisons between landslide statistics, digital elevation data, bedrock material properties, and earthquake ground motion (Frattini and Crosta, 2013; Valagussa et al., 2019; Jeandet et al., 2019).

The power-law distribution is widely used to describe the statistical distribution of large-area landslides (typically those >~1000 m²) in event-triggered inventories (e.g., Hovius et al., 1997; Guzzetti et al., 2002; Frattini and Crosta, 2013; Tanyas et al., 2017, 2018; Valagussa et al., 2019; Jeandet et al., 2019), as:

$$p(A) \propto A^{-\alpha} \tag{1}$$

where p(A) is the probability of observing a landslide of a given size, A, and α is the power-law scaling exponent. The concept of power-law scaling is supported by observations of highly nonlinear frequency-size statistics under an array of conditions, including for rainfall induced landslides (Guzzetti et al., 2002), co-seismic landslides (Tanyas et al., 2017 and references therein), large rock avalanches (Crosta et al., 2014), and even submarine landslides (ten Brink et al., 2006). As a theoretical framework, power-law scaling in landslides has garnered support due to the appealing analogy with Gutenberg-Richter scaling in earthquakes (Pelletier et al., 1997; Guzzetti et al., 2002) and conceptual consistency with the "sand pile" avalanches of cellular automata models (Liucci et al., 2017).

However, landslide distributions commonly only display power-law behavior over a small portion of their full range, often accounting for less than 25% of the total number of landslides in an inventory (Stark and Hovius, 2001). Typically, a decay in the frequency of smaller landslides creates a systematic deviation from power-law behavior at smaller scales. Early studies suggested that this reduction or "rollover" in frequency results from a sampling bias, where small landslides are censored below the resolution of the satellite or aerial imagery used for mapping (Hovius et al., 1997; Stark and Hovius, 2001; Brardinoni and Church, 2004). However, observation of a rollover continues even with the growing availability of high resolution (< 2m) imagery (Tanyas et al., 2017, 2018), suggesting that the rollover in these high-resolution inventories likely arises from physical factors. The smoothness of topography at scales smaller than the support area of channels (Pelletier et al., 1997), proportionally greater contribution of cohesive strength for shallow failure surfaces (Katz and Aharonov, 2006; Stark and Guzzetti, 2009; Frattini and Crosta, 2013), a non-linear shear-surface area to volume relationship (Milledge et al., 2014), and coalescence of small landslides through time (Tanyas et al, 2018) have been implicated as physical mechanisms that may inhibit failures on small slopes.

Despite consensus that the divergence from power-law scaling at smaller scales is not artificial, most landslide studies continue to devote great attention to the power-law scaling term, α (e.g. Tanyas et al., 2017, 2018; Vallagusa et al., 2019). We suggest that α alone provides only a narrow lens through which to view frequency size statistics for several reasons. First, because α is calculated only after discarding the potentially substantial portion of the landslide inventory that does not conform to power-law scaling, it is insensitive to the distribution of smaller landslides.

While the individual contribution to hazards and sedimentary budgets is lower for smaller landslides, they may still be significant to understanding the physical and mechanical constraints on landslide size distributions in general. Second, as a measure of the rate of decay in the frequency of landslides with increasing size, α indicates the relative abundance of large versus smaller landslides but conveys nothing specific about size. Two datasets could theoretically have the same α value while exhibiting no overlap in the range of absolute landslide sizes.

As an alternative to the use of power-law distributions, some authors have noted that some landslide size inventories are empirically consistent with the lognormal distribution (e.g., Kelsey et al., 1995; Evans 2003). Representing the exponentiated version of a normal (Gaussian) distribution, the lognormal distribution is a heavy tailed function with a finite mean and variance. This makes characterization with a lognormal distribution specific about the range of absolute values contained in the dataset, and also somewhat familiar due to the similarity with the common normal distribution.

In this study we investigate the utility of examining frequency-size datasets with the lognormal mean and standard deviation in landslide size. We first test the statistical agreement between the lognormal distribution and eight mapped inventories and then explore the physical and mechanical controls on landslide size through simulations and analysis of empirical inventories. We argue that the log-mean landslide size is strongly controlled by relief and rock strength, making the parameter useful to consider when comparing inventories from different landscapes.

2 Frequency-size scaling in co-seismic landslide inventories

2.1 Selection of inventories

Statistical comparison between landslide inventories is most instructive for datasets that share a common triggering mechanism and similar mapping standards. Compared to rainfall triggered or historic inventories, earthquake induced landslide inventories (EQIL) that meet these standards have become more available in recent years, with 66 digital inventories in the global database established by Tanyas et al. (2017). We therefore chose to focus exclusively on EQIL inventories in our study. Furthermore, we used metadata descriptions and our own evaluation against satellite imagery to select inventories that are close to complete down to the resolution of imagery used for mapping, with minimal amalgamation of adjacent landslides. As some censoring or amalgamation is unavoidable for landslides near the scale of the resolution used for mapping (Tanyas et al., 2018), we selected inventories with a modal peak much larger than the resolution-imposed limit (all selected inventories mapped from <5m imagery, except parts of the Wenchuan inventory, which was mapped at 10m). In total we identified eight inventories that met our criteria, which are shown in Figure 1. The majority of these inventories do not distinguish between source and runout area. We therefore use full landslide area for all the inventories except the Kaikoura dataset, where we consider the debris area because the available metadata did not link the source and runout polygons. Finally, to eliminate the statistical signature of failure mechanisms governed by different physics than soil/rock slides, we removed debris flows, induced lateral spreading, and large rock avalanches from each inventory. This primarily affected the Tohoku inventory which contains a significant number of lateral spreads, and the Gorkha inventory, where we removed the Langtang ice/rock avalanche.

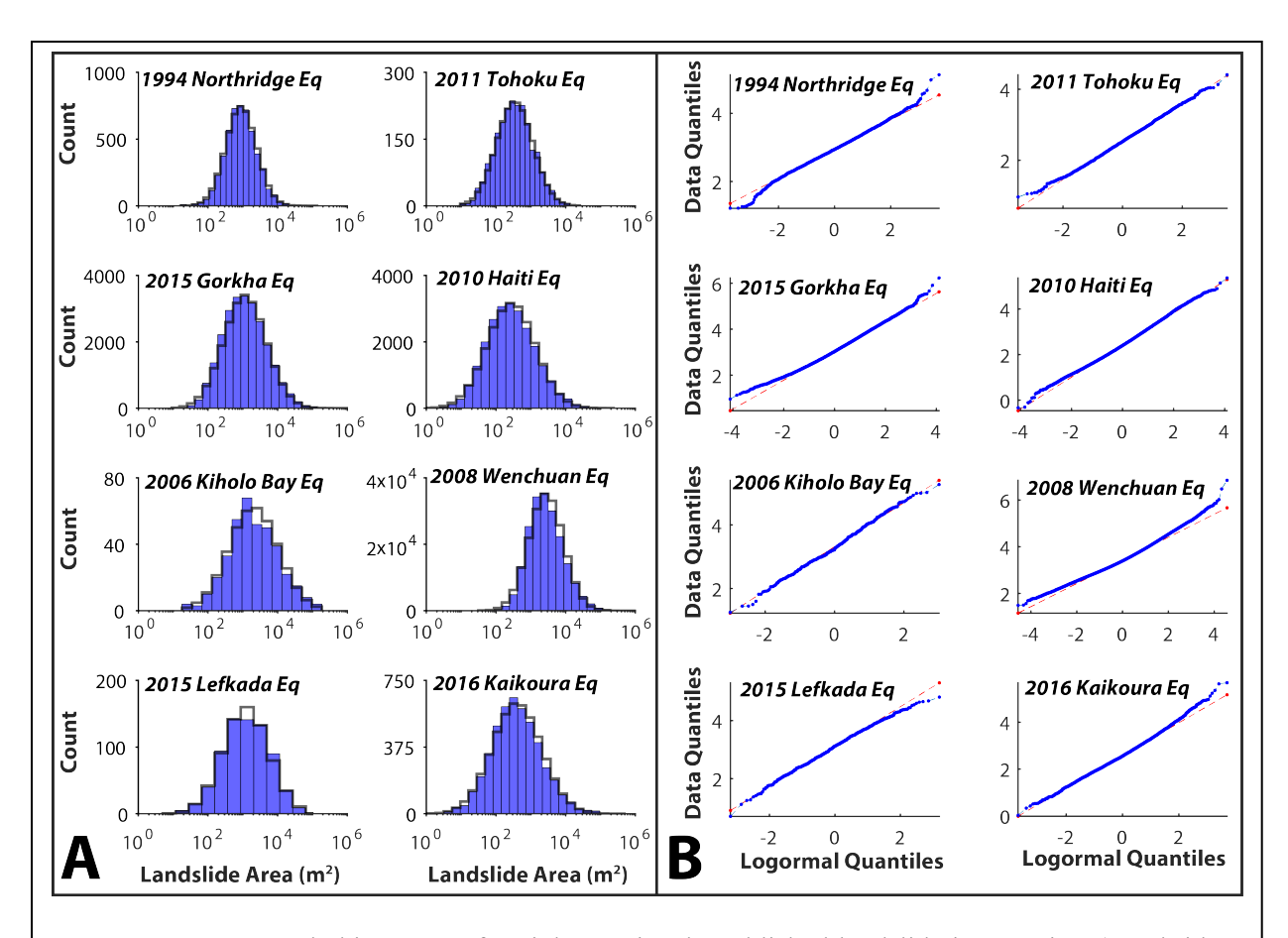


Figure 1: A) Log-scale histograms for eight previously published landslide inventories. (Northridge: Townsend et al., in revision; Tohoku: Wartman et al., 2013; Gorkha: Roback et al., 2018; Haiti: Harp et al., 2016; Kiholo Bay: Harp et al., 2014; Wenchuan: Xu et al., 2014; Lefkada: Clark and Zekkos, 2019; Kaikoura: Massey et al., 2018). Full landslide area (source and runout) is used to quantify size for all of the inventories except for Kaikoura, where debris area only is shown due to the lack of data for full landslide areas. The transparent histogram (black outline) plotted above the empirical landslide data (blue) displays a synthetic lognormal distribution with the same mean and variance as the data. **B)** Quantile-quantile plots comparing the inventories to the log-normal distribution. The log-scale quantiles of each inventory are plotted against the log-scale quantiles of a standard lognormal distribution. The points will plot on a straight line if the two distributions are similar.

We make a brief aside to highlight the versions of the 1994 Northridge inventory and 2015 Lefkada inventory we use in this study. These inventories were manually re-mapped to remove the amalgamation present in the original Harp and Jibson (1995) and Zekkos et al. (2017) versions respectively. Townsend et al. (in review) re-mapped the northern portion of the original Northridge inventory based on high-resolution aerial imagery and 3m digital topography. Their inventory contains 5064 landslides and covers approximately half the region of high density landsliding defined by Harp and Jibson (1995). The updated version of the 2015 Lefkada inventory is complete across the entire landslide effected region and contains 716 landslides (Clark and Zekkos, 2019).

2.2 A lognormal approach to frequency-size datasets

Figure 1A shows frequency-area distributions for the eight selected co-seismic inventories as log-

scale histograms. We show histograms rather than the empirical probability density estimates common in landslide studies because the bin value (count) is not skewed by the bin size as it is for probability density. This property of histograms highlights the finite mean and variance in the inventories, which is qualitatively consistent with the lognormal distribution. As a more rigorous test for lognormality, the quantile-quantile plots in Figure 1B compare the quantiles of each inventory to those predicted by a standard lognormal distribution. While generally strong linearity in these plots supports a statistical match, we note that positive skewness in the Gorkha, Wenchuan, and Kaikoura inventories create a systematic deviation from the lognormal predictions to a degree that is unlikely to be explained as statistical noise.

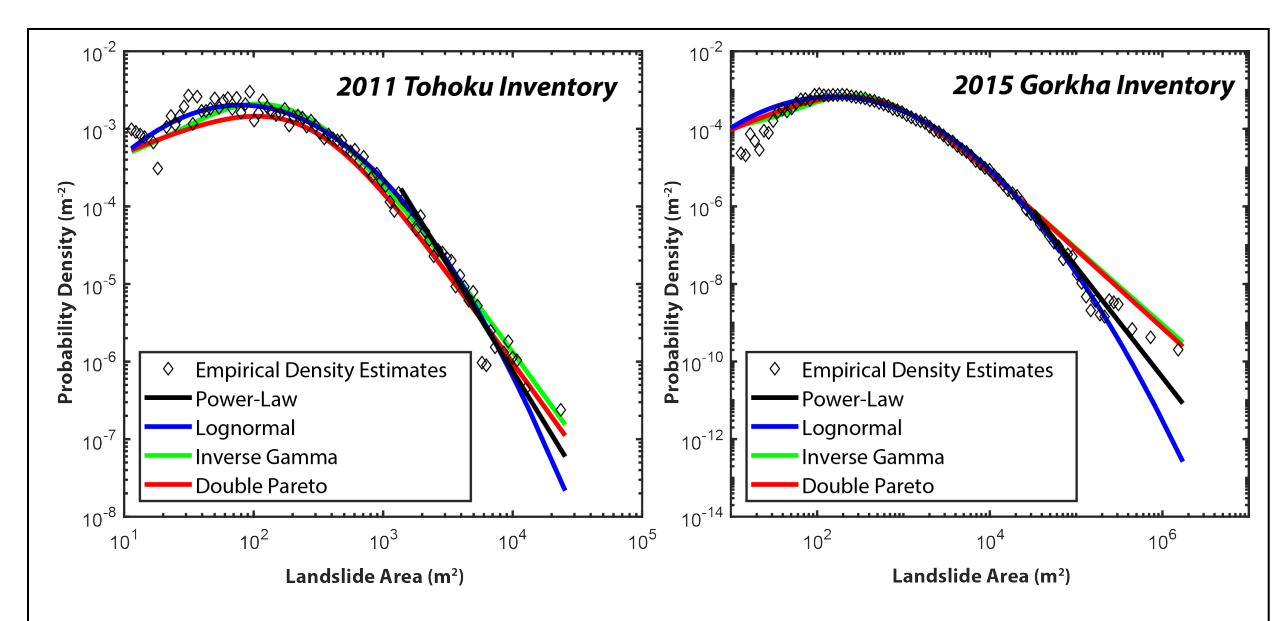


Figure 2: Comparison between log-normal and power function fits to the density estimates of landslide size for the 2011 Tohoku inventory (Wartman et al., 2013) and the 2015 Gorkha Inventory (Roback et al., 2018). These two datasets show endmember misfit to a lognormal distribution. Power-law parameters were estimated using the principled approach developed by Clauset et al. (2009), which combines maximum likelihood estimation and goodness-of-fit tests to identify the lower bound to power-law scaling.

One explanation for the deviation from lognormal scaling may be an incomplete removal of amalgamation or deep-seated failure modes in the Gorkha, Wenchuan, and Kaikoura inventories. Alternatively, the lognormal distribution may not be the 'true' underlying statistical distribution. Previous studies have argued for the general applicability of the power-law, inverse gamma, and double Pareto distributions (Hovius et al., 1997; Malamud et al., 2004; Stark & Hovius, 2001). Figure 2 compares the maximum likelihood model fits between the lognormal distribution and these alternative heavy-tail functions for the 2011 Tohoku and 2015 Gorkha landslide inventories (see supplementary Figures S1-S8 for the remaining six inventories). This analysis shows a qualitatively similar statistical agreement between all four distributions. However, a rigorous statistical selection between models is not our intent; all four of the distributions in Figure 2 have been shown to provide accurate empirical predictions (Power Law: Hovius et al., 1997; Guzzetti et al., 2002; Tanyas et al., 2017; Double Pareto: Stark and Hovius, 2001; Inverse Gamma: Malamud et al., 2004; Lognormal: Kelsey, 1995; Evans, 2003), and all may be useful depending on the context. Instead, our main point is that the lognormal fits are comparable to the alternative

distributions, and critically, that the lognormal distribution quantifies the finite mean and variance observed in landslide frequency-size datasets. In this context, the lognormal is a parsimonious distribution that conveys scale-specific information about landslide size. We focus on log-scale mean and standard deviation statistics for the remainder of this study because our goal is to explore how slope instability is favored or censored at specific length scales.

3 Controls on landslide size in a synthetic inventory

To explore the mechanisms that can generate the observed landslide distributions, in this section we conduct simulations of earthquake-induced landslides and then relate model parameters back to the resulting landslide size statistics. Previous studies have suggested that topographic characteristics, hillslope material strength, and seismic loading are important controls on landslide size (Frattini and Crosta, 2013; Valagussa et al., 2019, Jeandet et al., 2019). We therefore focus on these parameters in our simulations.

3.1 Methods

We simulate landslide distributions by measuring hillslope geometries from a digital elevation model (DEM) and then assessing the stability of each hillslope using a limit equilibrium (LE) slope stability model. We incorporate pseudostatic seismic conditions in order to explore the effect of variable seismic loading. Synthetic landslides are identified as unstable hillslopes (Factor of Safety < 1), and frequency-size statistics are returned in terms of landslide length. We use length as a proxy for landslide area because our measurements of hillslope geometry are restricted to 2D (height and slope only). Finally, we validate our approach by comparing simulated versus observed landslides associated with the Northridge earthquake.

Our DEM measurements of hillslope geometry rely on a variation to the conventional derivation of digital channel networks, which are commonly determined from hydraulic flow routing algorithms and a user-defined threshold contributing drainage area that defines channel initiation (Montgomery and Foufoula-Georgiou, 1993). While channels are commonly defined as DEM grid cells that correspond to a contributing drainage area greater than 10⁶ m², we define hillslopes as grid cells with less than 5x10⁴ m² of support area (roughly the contributing area for colluvial channels; Montgomery and Foufoula-Georgiou, 1993; Whipple and Tucker, 1999). We use a threshold representative of colluvial channels because the majority of landslides are smaller than the ridge-main-stem-channel distance, and we want to ensure that our slope measurements cover these smaller scales. We then use the D8 flow model (O'Callaghan and Mark, 1984) to create flow paths along hillslopes. Following the approach of other recent studies (Townsend et al., in review; Grieve et al., 2016), we use the slope angle and height defined by these hydraulic flow paths as simplified hillslope geometries for slope stability analysis (Figure 3). Although the majority of hillslope flow paths have a single start and end point, convergent topography does result in some multi-branch flow paths. In these instances, we use the height and slope between the overall highest and lowest points on the flow path.

While the 2D geometries generated by our approach provide more information than pixel-based slope alone, it is important to note that the hillslope flow paths do not necessarily represent the only location where a landslide could form. Surface roughness or minor breaks in slope may facilitate landslides smaller than the flow distance defined by a constant support area. However, a more complete search for the most critical slope patches would be computationally challenging to

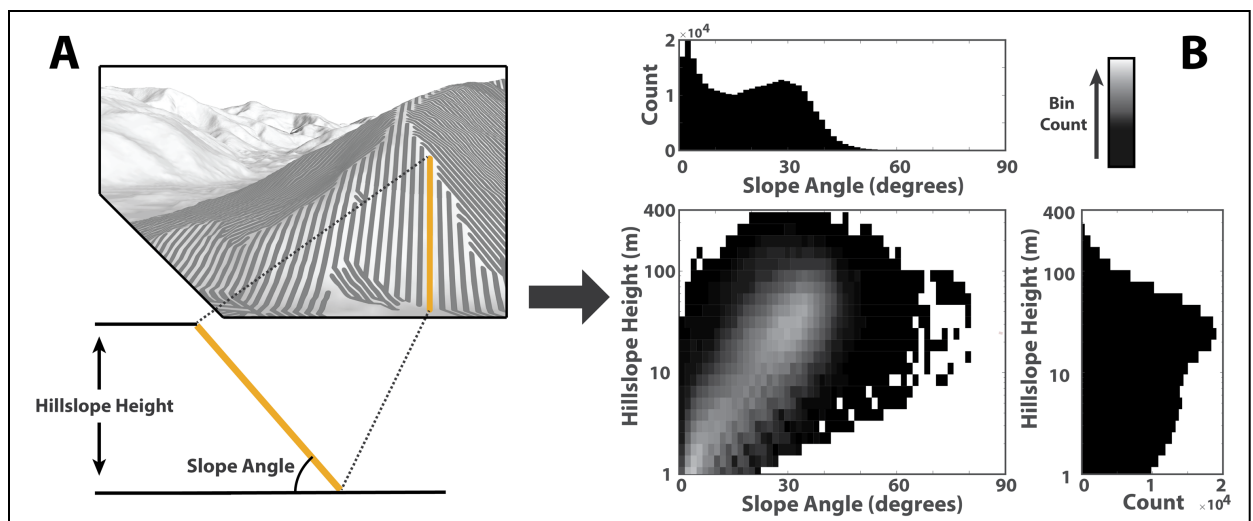


Figure 3: Illustration of our approach to measuring hillslope geometry from a DEM. **A)** Flow direction and accumulation algorithms delineate hydraulic flow paths on hillslope grid cells, which are defined by flow accumulation values less than the threshold for channel initiation. These flow paths provide a simplified hillslope geometry consisting of a slope angle and height. **B)** Applying this technique to the entire DEM results in a distribution of hillslope geometries, which can then be assessed for slope stability using limit equilibrium (LE) analysis (e.g. Fig. 4).

implement at landscape scales. We therefore only consider the possibility that each 2D hillslope profile fails along the entire distance, with the length along the failure plane corresponding to the resulting landslide length (Figure 4).

To assess the stability of each hillslope measurement, we consider forces acting on a planar wedge failure geometry (Culmann, 1875). We apply a pseudostatic formulation of Culmann's analysis (Ling et al., 1999), where seismic acceleration is portrayed as a permanent horizontal body force added to the hillslope's free-body diagram (Figure 4). We do not consider vertical accelerations because they are not generally dominant (Campbell and Bozorgnia, 2003) and are not reported in USGS ShakeMap estimates. The pseudostatic Culmann analysis provides an analytic bounding relationship between slope gradient and hillslope relief, such that the maximum stable hillslope height is given by:

$$H_{crit} = \frac{4c\cos\theta\cos\varphi\sin(\alpha)}{\gamma[1-\cos(\varphi-\alpha-\theta)]} \tag{2}$$

where c is cohesion, φ is the material's friction angle, γ is the material's unit weight, and α is the slope angle. Slopes taller than the critical height, H_{crit} , correspond to a Factor of Safety <1, and are predicted to fail. The factor θ is given by:

$$an \theta = k_h \tag{3}$$

where k_h is the pseudostatic coefficient, which determines the magnitude of the pseudo horizontal force on the sliding wedge (representing the force generated during an earthquake). Pseudostatic coefficients are generally selected to be some fraction of the peak ground acceleration (PGA) to account for the fact that peak acceleration occurs only briefly and does not create a unidirectional

or synchronous loading throughout the sliding mass (Hynes-Griffin and Franklin, 1984; Jibson, 2011). We use this approach in our preliminary test simulations (section 3.2), where we linearly scale k_h to the USGS *ShakeMap* PGA estimates. For simplicity in our parameter space exploration (section 3.3), we set k_h equal to 1.0, and scale PGA values from 0-0.5 g (see Figure 6).

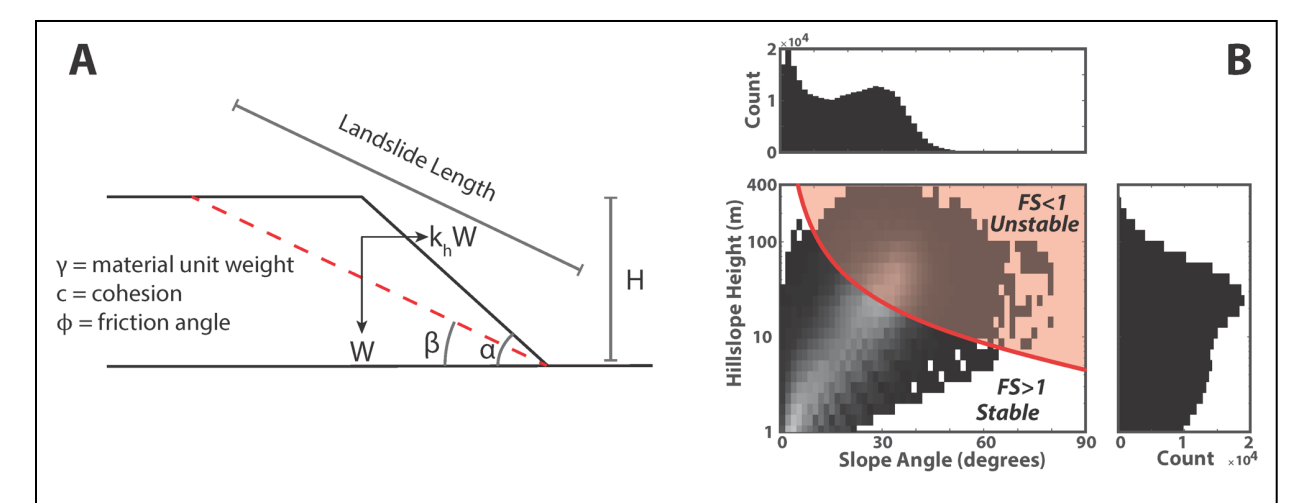


Figure 4: A) Force diagram for the pseudostatic extension of Culmann's sliding wedge analysis. Hillslopes larger than the maximum stable height, H_{crit} , are predicted to fail. Dynamic seismic loading is simplified as an additional horizontal force, $k_h \cdot W$, where W is the weight of the sliding wedge and k_h is the seismic coefficient. **B)** For uniform parameters, Culmann's analysis provides a bounding relationship between hillslope height and slope. Hillslopes plotting above the red curve are predicted to fail as landslides (FS<1), while those below the red curve are predicted to be stable (FS>1).

3.2 Model Validation

While an inversion for strength parameters is beyond the scope of this study (cf. Gallen et al., 2015), we compare our model simulations against a real co-seismic landslide inventory to verify that it produces a comparable statistical distribution given realistic strength parameters. We use the 1994 M_w6.7 Northridge Earthquake inventory as a test case because the local hillslopes are steep, moderately tall (~100m), and planar, which are conditions where Culmann's analysis is closest to more rigorous limit equilibrium methods that assume log spiral geometries (Ling et al., 1999). We simulate landslides using a 3 meter IfSAR DEM (OCM Partners/NOAA, 2004), and hillslope material properties representative of those reported by Dreyfus et al. (2013) for the landslide affected region ($\varphi = 30^{\circ}$, cohesion = 12 kPa, unit weight = 15.7 kN/m³). Furthermore, we allow for a spatially variable seismic coefficient, scaling the value of kh to 50% of the USGS ShakeMap PGA estimates for the Northridge Earthquake (contributed by ATLAS: last updated 2017-04-12 06:25:42 (UTC)), which is the value suggested by Hynes-Griffin and Franklin (1984). Finally, for comparison to the 2D model predictions, we use the Northridge inventory by Townsend et al. (in review), who re-mapped the northern portion of the original inventory by Harp and Jibson (1995) to remove the effects of amalgamation. We calculate landslide length for the mapped Northridge landslides using a simplified polygon enclosure to estimate distance along the runout axis (minimum bounding geometry tool, ArcMap 10.6).

Figure 5 compares the predicted and observed landslide inventories. The large number of synthetic failures reflects the flow-routing technique used to measure hillslopes; groupings of adjacent 2D

flow paths predicted to fail correspond to single landslides in a real landscape. The two inventories show close agreement in terms of frequency-length statistics (Figure 5A), with geometric mean sizes (i.e. 10^{μ} , where μ =mean(log₁₀(length))) of 65 m vs 58 m for the synthetic and empirical inventories respectively. Visual inspection of the quantiles in Figure 5B shows consistency between both inventories and a lognormal distribution over the full range of values. Thus the model accurately reproduces the observed size statistics, which are the focus of attention here.

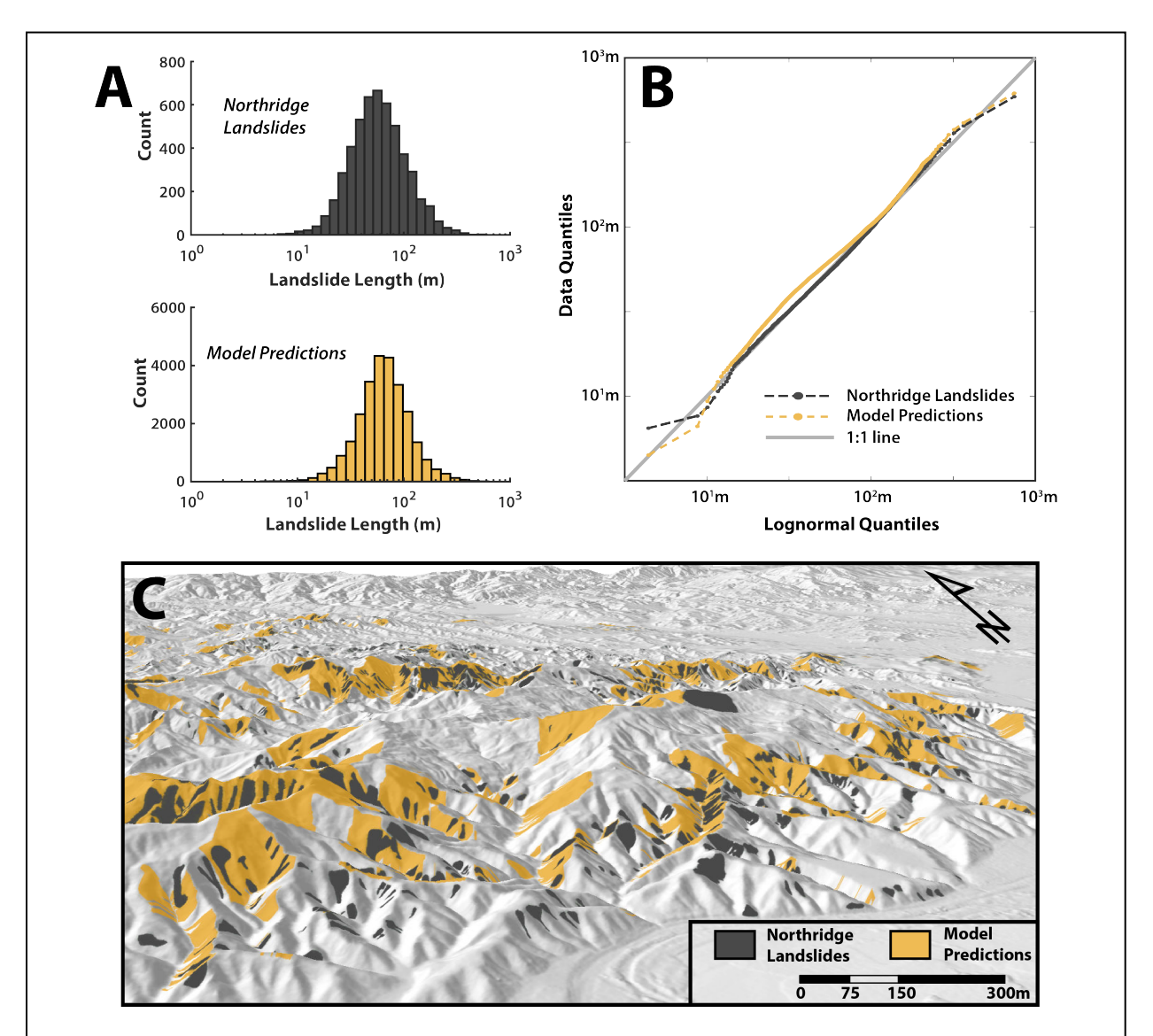


Figure 5: Comparison between the mapped Northridge frequency-length distribution and a synthetic distribution using model parameters of $k_h = 0.5 \cdot PGA$, unit weight = 15.7 kN/m³, $\phi = 30^\circ$, and cohesive strength of 12kPa. These model parameters produce similar frequency-size statistics to the real Northridge inventory (**A** and **B**). Compared to the mapped inventory, the larger number of synthetic failures in **A** is a consequence of the flow-routing technique used by this study to measure hillslopes. Model landslides correspond to individual hillslope segments that are only one-pixel (3m) wide, and many adjacent segments may correspond to a single landslide in a real landscape (see clustering of failed hillslope segments in **C**).

3.3 Parameter Space Exploration

In a series of simulations, we impose variations in PGA (where k_h =1•PGA) and the cohesive strength of hillslope material, assuming a friction angle and unit weight of 30° and 15.7 kN/m³ respectively. Two examples are presented using a 3m DEM for the region affected by the 1994 Northridge Earthquake in California (IfSAR-derived product; OCM Partners/NOAA, 2004), and a 30m DEM for the region affected by the 2015 Gorkha Earthquake in Nepal (SRTM-derived product; Farr et al., 2007). We select these two regions in particular as they are endmembers in terms of topographic relief amongst the locations from Figure 1.

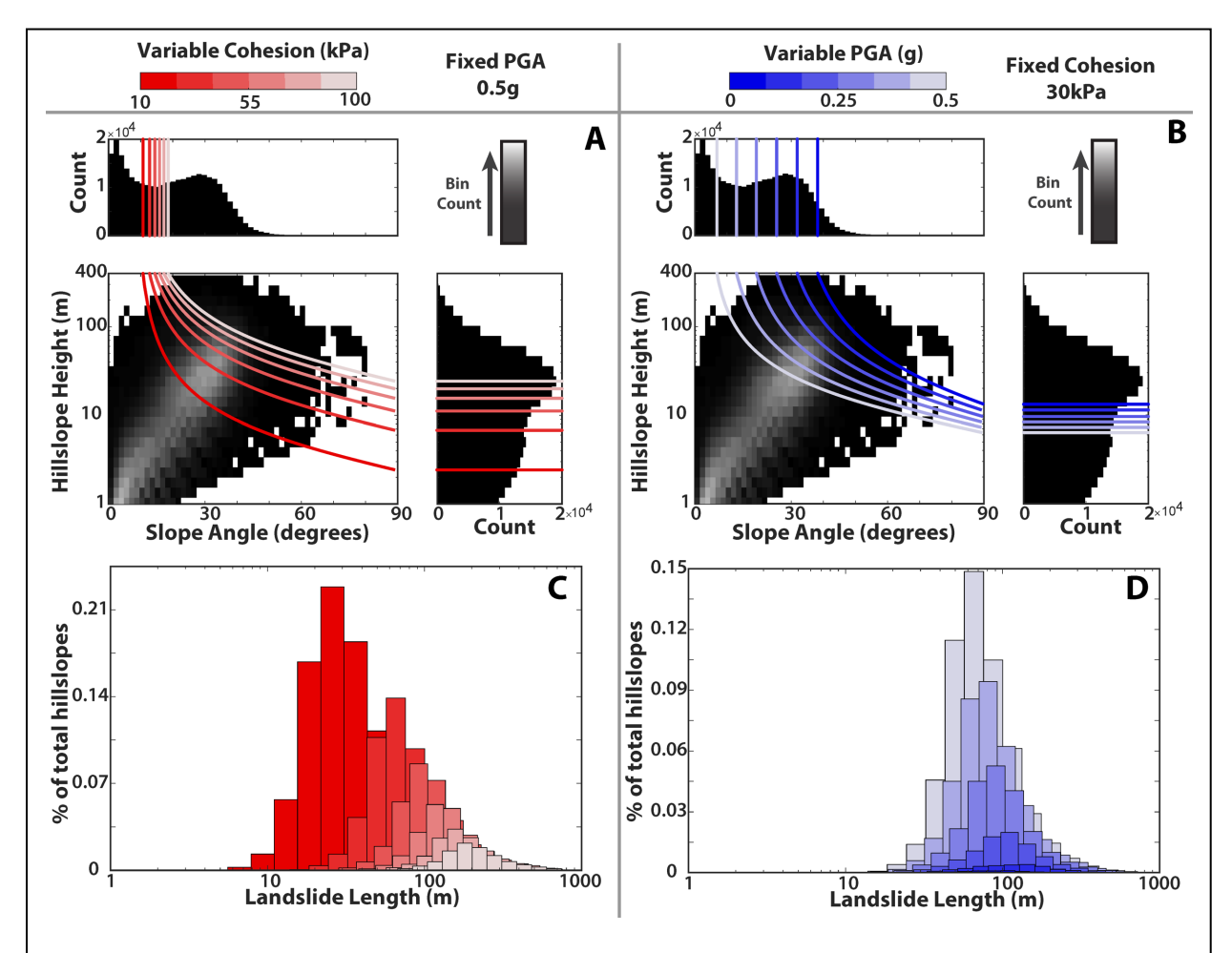


Figure 6: Landslide simulations for the region affected by the 1994 Northridge earthquake (southern California). Bivariate distributions (slope angle and height) of hillslope geometries are measured from a 3 m DEM, where lighter colors represent higher data density. The curves define FS=1 for different values of cohesion (**A**), and PGA (**B**). Hillslopes that plot above the curves (i.e. taller, steeper slopes) are predicted to fail (see Fig. 4), resulting in the landslide size distributions shown in the bottom panels (**C**, **D**). The height of the histograms quantifies the percentage of failed hillslope profiles out of the total number measured from the DEM.

The bivariate histograms for the Northridge simulations display a cross-tabulation of slope angle and hillslope height for all of the hillslopes measured from the 3m DEM, showing peak modal values of 30° slope and 50 m hillslope height (Figure 6A and 6B). However, hillslope height and

slope distributions are not symmetrically distributed and instead show a second peak of values for very low slopes and short hillslope segments, which represents roughness largely owing to anthroprogenic structures recorded by the 3m IfSAR data. Superimposed on the hillslope distribution are the bounding curves defined by Culmann's stability analysis (FS = 1) for a range of cohesion (Figure 6A) and PGA (Figure 6B) values. Hillslopes plotting above the curves (i.e. taller and/or steeper slopes) are predicted to be unstable for the choice of parameters. Landslide size is quantified as the length of the failure plane through each unstable hillslope, which results in the landslide distributions shown in Figure 6C and 6D.

The stability curves defining FS=1 in Figure 6A reveal how increases in cohesion increase the critically stable hillslope height to a greater degree than increasing the critical slope gradient. This effect is highlighted by the spacing of the curves, which are more widely spaced along the vertical axis (height) compared to the horizontal axis (slope). Physically, the pronounced relationship between cohesive strength and critical hillslope height can be explained by the fact that any non-zero cohesive shear resistance will compensate the gravitational driving force on sufficiently small sliding masses, regardless of frictional strength. Thus increasing model cohesion increases the threshold (minimum) hillslope height required for the failure of a given slope gradient (curves extended onto the 1D histogram of hillslope height correspond to a 90° slope, Figure 6A). As a result, the predicted landslides are increasingly restricted to the tallest subset of hillslopes, which causes larger landslides on average and a narrower distribution of hillslope heights, i.e., smaller standard deviation (Figure 6C).

In contrast, increases in PGA more strongly affect the critical slope gradient required for failure compared with the critical height (Figure 6B). This result is a physical consequence of the fact that seismic loads are modeled as horizontal forces, which reduces shear resistance to a greater degree on steeper slopes compared to flatter ones. While vertical accelerations do specifically penalize slope height in the Ling et al. (1999) analysis, we highlight that the horizontal component dominates in empirical data (Campbell and Bozorgnia, 2003). In terms of landslide frequency-size statistics, the primary result of increasing PGA is the generation of landslides over a greater range of length scales (i.e. increasing standard deviation; see widening of the histograms in Figure 6D). However, we also note a subtle decrease in average size with increasing PGA, reflecting the relative abundance of smaller hillslopes that only become unstable at high PGA. For example, PGA greater than ~0.25g allows for failure of the most frequent hillslope geometry in the Northridge DEM, which is around ~30° steep and ~50 m tall (i.e. PGA contours reach the peak of the histogram in Figure 6B for values greater than 0.25g). This result highlights the role of topography in determining landslide frequency size statistics. While increasing seismic loads mechanically permit the failure of an increasing range of hillslope geometries, the spatial distribution of strong ground motions in a real earthquake restricts the availability of hillslopes to particular sizes, which provides an independent constraint on what landslide sizes are possible and most likely.

Figure 7 shows the same parameter space exploration for the topography affected by the 2015 Gorkha Earthquake in central Nepal (Himalayan Mountains), where the principal difference from the Northridge simulations is the order of magnitude increase in the maximum hillslope relief. In this landscape, we observe a unimodal distribution of both slope and hillslope length with peak values around 35° and 200 m respectively. Due to the higher relief in Nepal, we used a -

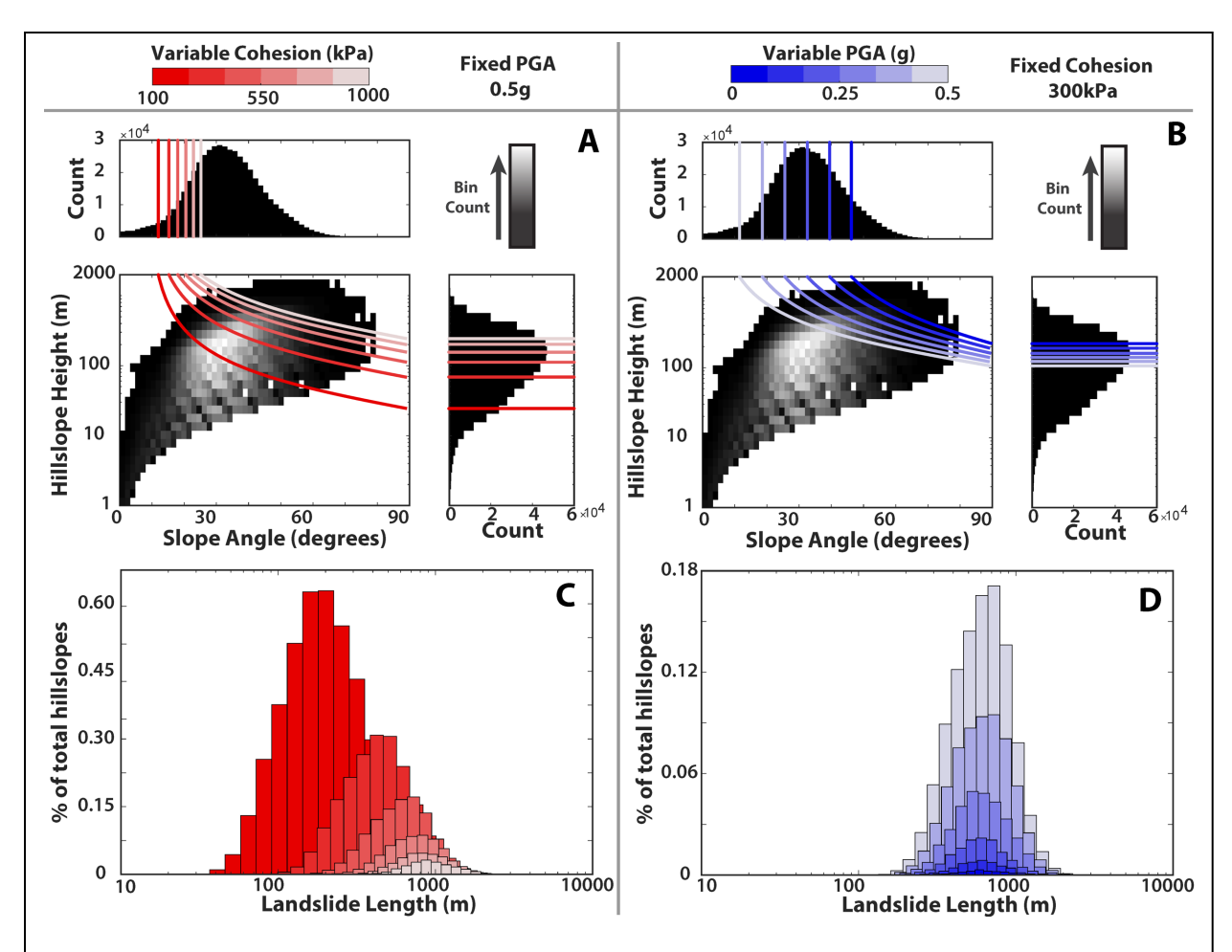


Figure 7: Landslide simulations for the region affected by the 2015 Gorkha earthquake (central Nepal). Bivariate distributions (slope angle and height) of hillslope geometries measured from the 30m DEM, where lighter colors represent higher data density. The lower cutoff to the bivariate distribution results from the fact the that horizontal distance along hillslope flow paths (i.e. $H/\tan(\alpha)$) can only take on integer values in multiples of 30m for the 30m resolution DEM. The curves define FS=1 for different values of cohesion (**A**), and PGA (**B**). Hillslopes that plot above the curves (i.e. taller, steeper slopes) are predicted to fail (see Fig. 4), resulting in the landslide size distributions below (**C**, **D**). The height of the histograms quantifies the percentage of failed hillslope profiles out of the total number measured from the DEM.

correspondingly higher range of cohesive strength relative to Northridge in order to achieve static stability (<0.2% of all hillslopes predicted to fail at C=100 kPa, PGA = 0). In general, we observe the same scaling behavior described previously for our Northridge simulations, where decreasing cohesion and increasing PGA both result in more total landslides. Also similar to the first example, increasing cohesion significantly increases mean landslide size, while also decreasing the standard deviation of landslide size (Figure 7C). Increasing PGA primarily increases the range of landslide sizes, although for the Nepal simulations we observe a subtle shift to slightly larger average landslide sizes, opposite of the Northridge example (Figure 7D). As noted previously the effect of PGA on landslide size depends on the availability of hillslopes. Unsurprisingly, the abundance of hillslopes many hundreds of meters in height allows for larger landslides in Nepal compared to

Northridge. However, it is difficult to separate the effect of relief alone, as hillslope-scale relief and rock strength exhibit a co-variance under the assumption of Culmann's model (Schmidt and Montgomery, 1995). Indeed, higher slope cohesion is required to prevent an unrealistic number of landslides for our simulations in the higher relief Nepal landscape (up to 1MPa, Figure 7), and, as we have now shown, increasing cohesion also predicts an increase in average landslide size because it censors shorter and less steep slopes from the distribution.

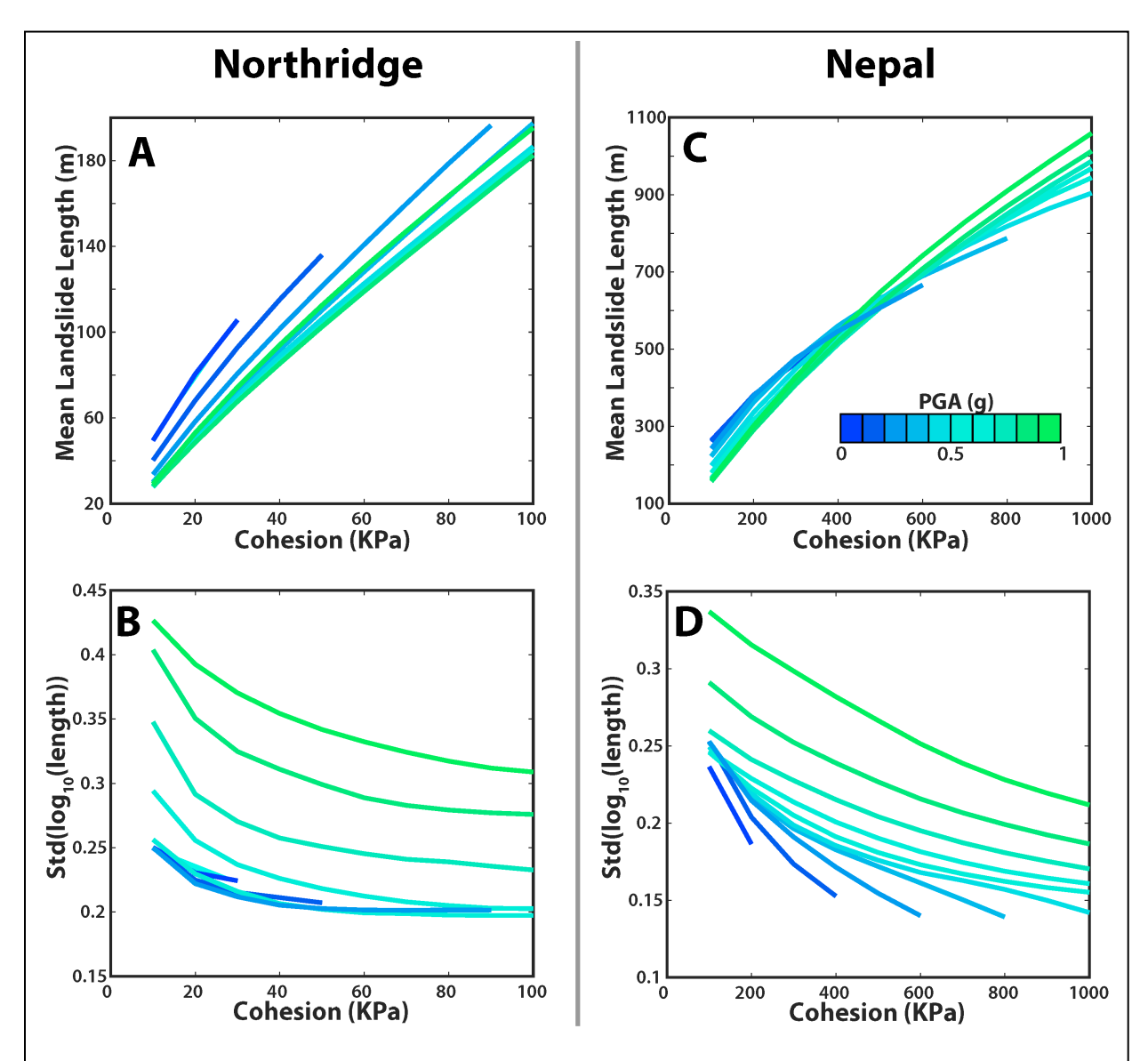


Figure 8: Landslide length statistics for simulations using a range of values for cohesion and PGA, and digital topography from Northridge ($\bf A$, $\bf B$) and Nepal ($\bf C$, $\bf D$). Geometric mean landslide size (i.e. 10^{μ} , where $\mu = \text{mean}(\log_{10}(\text{length}))$) increases with increasing cohesion ($\bf A$, $\bf C$), while the log-transformed standard deviation in landslide size decreases with increasing cohesion ($\bf C$, $\bf D$). The standard deviation in landslide size generally increases with increasing PGA, but the effect of PGA on the mean size depends on the landscape and the value for cohesion ($\bf B$, $\bf D$), with differences in topography between the two sets of simulations influencing specific landslide scaling behavior.

Figure 8 summarizes predicted landslide length (geometric mean and standard deviation) for all combinations of cohesion and PGA, for both the Northridge and Nepal examples. Increasing cohesion for both landscapes produces a nearly linear increase in geometric mean landslide length (Figure 8A, 8C) and a non-linear decrease in the log-scale standard deviation of landslide size (Figure 8B, 8D). Both of these effects reflect the stability of increasingly larger hillslopes as cohesion increases, thus restricting the distribution of landslide size to larger and more narrowly distributed values (on a log scale). For increases in PGA, we find that the primary result in both the Northridge and Nepal simulations is an increase in the log standard deviation in landslide size (Figure 8B, 8D), and a decrease in the total number of landslides generated (the curves become truncated at low PGA and high cohesion values because no landslides are predicted under these conditions). Differences in the exact response to PGA between the two sets of simulations highlight the role of topography in determining landslide statistics. For example, while we find that geometric mean landslide length systematically decreases with PGA at low cohesion values and increases with PGA at higher cohesion values for both sets of simulations, the value of cohesion at which this transition occurs is unique to the landscape (i.e. the crossing, or bending over of contours in Figure 8A, 8B). Furthermore, while the log-scale standard deviation generally increases with increasing PGA for both sets of simulations (Figure 8B, 8D), the increase is negligible in the Northridge simulations below 0.5g (i.e. stacking of the contours in Figure 8B), but present for all values of PGA in the Nepal simulations. The simulations for the two landscapes are particularly different at low values of PGA because relatively few landslides are activated under these conditions, making the underlying hillslope distribution especially important in determining landslide size statistics.

4 Controls on landslide size in empirical inventories

Our simulations highlight rock strength, hillslope-scale relief, and ground motion intensity as important physical parameters that affect the distribution of landslide size. Our modeling results suggest landslides will be larger on average in regions with greater available hillslope relief and/or higher cohesive strength. Furthermore, increasing PGA is predicted to increase the range in landslide sizes. In this section we test for these effects in empirical data, using the mapped inventories from section 2 along with the corresponding *ShakeMap* PGA datasets and DEMs.

4.1 Influence of hillslope relief on landslide size

In this section, we compare landslide size statistics to hillslope relief in two different ways. First, to view the variance within each inventory individually, we binned the landslide distributions by the local relief estimated at the location of each landslide. We estimated hillslope relief using the same technique we used to extract hillslope geometries for stability analysis in section 3.1, where we measured the vertical offset on flow paths with support areas no larger than $5x10^4$ m². We then converted our hillslope relief estimates to rasters with grid cell values representing the total relief on the flow path passing through each cell (see supplementary table S1 for DEMs used in this analysis, and Figures S11-18 for hillslope relief maps for each region). Finally, we binned the landslide distributions by the relief estimated at the centroid of each landslide and computed the log-scale mean landslide size for relief bins that contain at least 20 landslides (Figure 9A).

As a second approach, we compared the inventories against each other with a single set of mean and standard deviation statistics representing the entirety of each landscape (Figure 9B, 9C). Such a comparison of relief between landscapes becomes sensitive to the threshold drainage area that -

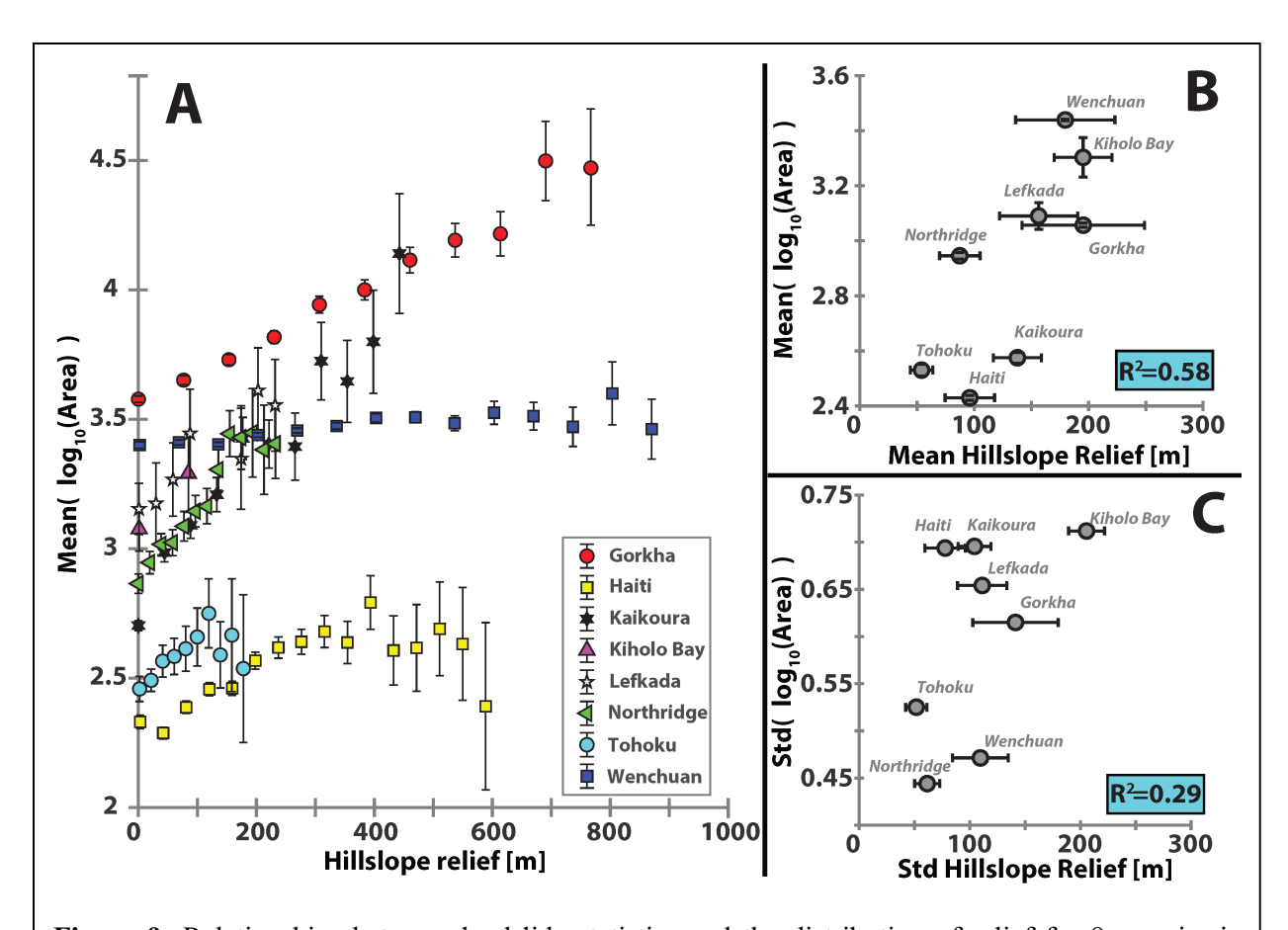


Figure 9: Relationships between landslide statistics and the distribution of relief for 8 co-seismic landslide inventories. **A)** Log-averaged landslide size as a function of relief within each landscape individually. Vertical error bars are the 95% confidence interval on the mean for each bin. **B)** A similar relation to **A)** holds between landscapes, when landslide size and relief are averaged for the whole event. Horizontal error bars are the standard deviation between 100 estimates for different threshold drainage area values. Vertical error bars are the 95% confidence interval on the mean landslide size for each landscape. Due to the large number of data in each inventory these error bars are tightly constrained. **C)** The log-transformed standard deviation in landslide area shows a positive relationship with the standard deviation of relief, suggesting that more variable hillslope sizes allow for more variable landslide geometries. Horizontal error bars again represent the standard deviation between estimates for different threshold drainage area values.

defines the hillslope regime, since this value is known to vary between landscapes (Montgomery and Foufoula-Georgiou, 1993; Whipple and Tucker, 1999). However, slope area analyses for the DEMs we used did not reveal a clear rollover in the slope-area relationship indicative of the hillslope drainage threshold (Figure S9). We therefore chose to account for uncertainty in the drainage threshold by using a range of values for each landscape. Using 100 log-uniformly distributed threshold drainage area values between 10⁴ and 10⁵ m², we generated an ensemble of 100 hillslope relief rasters for each landscape. We then calculated the mean and standard deviation in relief among the grid cells of each raster and averaged the statistics between the 100 estimates for each landscape. This sensitivity analysis quantifies how our hillslope relief statistics depend on the choice of the threshold contributing area value. The horizontal error bars in Figure 9B and 9C are the standard deviation in relief statistics for the ensemble of drainage thresholds. See

supplementary section S2 for the full sensitivity analysis.

For variations within a single landscape (Figure 9A), we found that landslide size systematically increases in the hillslope relief bins. Partial correlation coefficients computed with bin count as the control variable are statistically significant (p<0.05) for every dataset in Figure 9A except the Lefkada and Kiholo Bay inventories, which only contain 7 and 2 bins with at least 20 landslides respectively. We also found that different landscapes show different landslide sizes for the same values of relief, potentially reflecting differences in average rock strength or a bias introduced by using the same drainage threshold for each landscape. For variations between landscapes, we found a positive relationship ($R^2 = 0.58$) between the overall log-scale mean landslide size and mean hillslope relief (Figure 9B), and a weaker relationship ($R^2 = 0.29$) between the log-transformed standard deviation in landslide area and the standard deviation of hillslope relief (Figure 9C).

While the empirical correlation between landslide size and relief in Figure 9 is consistent with the expectation from our simulations, the underlying mechanism is less clear. High relief topography is likely associated with higher rock strength at the scale of individual hillslopes (Schmidt & Montgomery, 1995; Townsend et al., in review), and we have already demonstrated that a larger sliding mass is required to achieve critical conditions in a stronger medium (Figures 6,7,8). On the other hand, our use of full initiation and runout area for the analysis in Figure 9 leaves open the possibility that the correlation to relief simply reflects the greater runout distance available on longer slopes, independent of initiation area. Furthermore, correlation between the size of the sliding mass and runout area is well established (Roback et al., 2018), suggesting that a combination of factors is likely. Nonetheless in practical terms, the relative importance of hillslope strength and space for runout matters little because both factors correlate to relief and also act to increase landslide size. The strong relationships in Figure 9 indicate relief is a first order predictor of landslide size and underscore how landslide statistics reflect the local geomorphology.

4.2 Influence of PGA on landslide size

For each of the eight empirical landslide inventories, we categorized the mapped landslide polygons based on PGA contours taken from the USGS *ShakeMap* ground motion estimates. We constructed PGA bins such that at least 20 landslides fall into each bin. We excluded the 2015 Lefkada landslide inventory because the range in PGA across the landslide affected coastline was <0.2g.

Figure 10 displays the log-scale mean and standard deviation in landslide size for each bin, plotted against the average PGA for that bin. For each set of bins, we computed the partial correlation between PGA and the bin value while controlling for the sample size represented by the bin. Regressions are shown for datasets where a Student's t-test for the significance of the partial correlation coefficient rejects the null hypothesis of zero correlation (p<0.05). In contrast to our simulations reported in Section 3, we find no systematic trend between PGA and the log-scale standard deviation in landslide size. However, we do observe weak but statistically significant negative correlations between the log-scale mean size and PGA for 3 of the larger inventories, which is consistent with the predictions of our simulations for lower values of cohesion (Figure 8A, 8C).

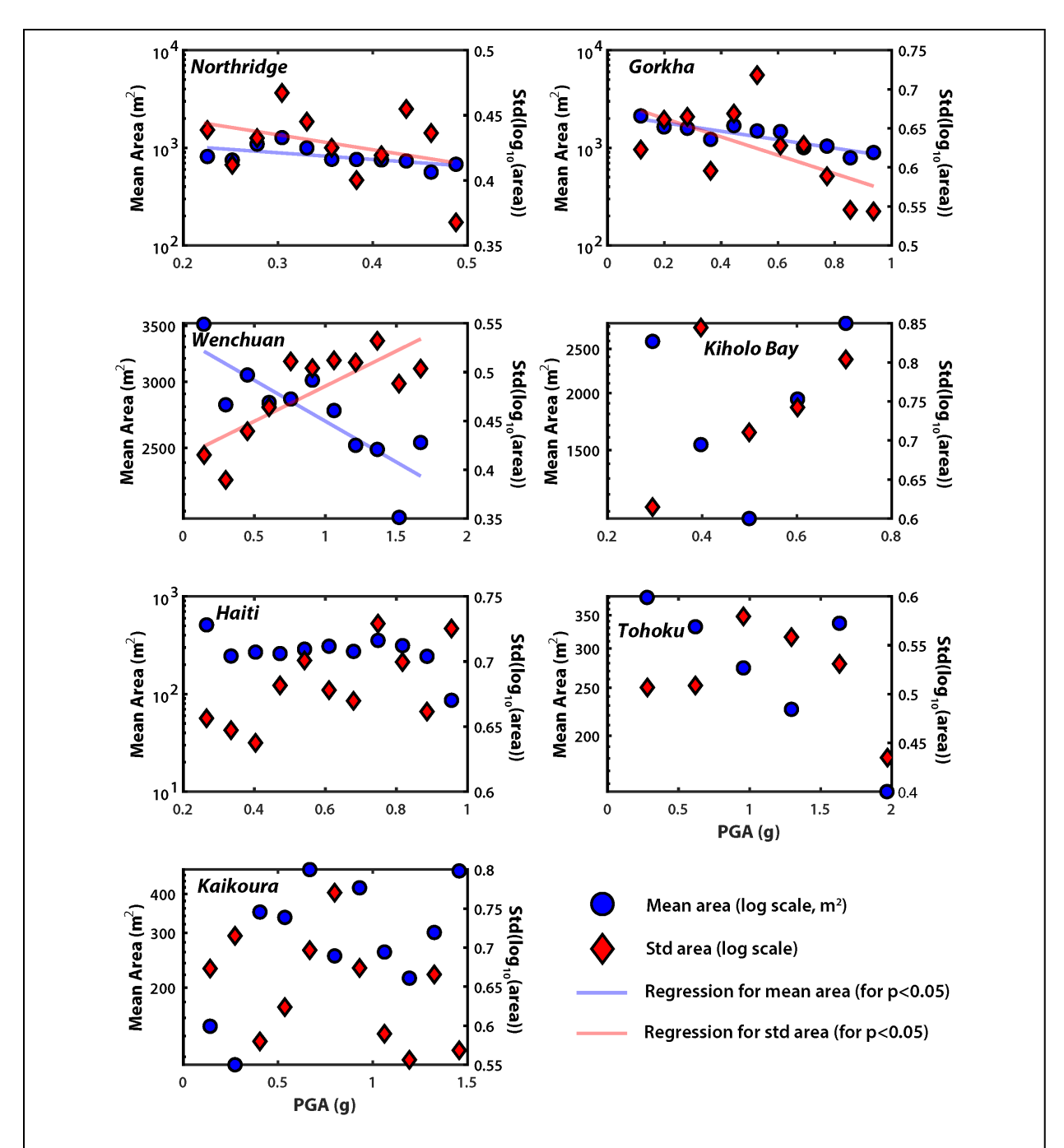


Figure 10: Relationships between geometric mean and standard deviation in landslide size and *ShakeMap* PGA estimates for seven co-seismic inventories. Regressions are shown for the datasets where the partial correlation between mean/std landslide size and PGA while controlling for bin count are significantly different from 0 (p<0.05). A comparison of landslide size versus average PGA across the sites in this study (similar to that for relief in Fig. 9) is not meaningful because overall mean PGA does not vary much between the different earthquake events.

Valagussa et al. (2019) found a weak negative correlation between the frequency-area power-law scaling exponent and PGA for 3 of the 6 inventories they investigated, which may be consistent

with our results. Interestingly, the strongest relationship Valagussa et al. (2019) found between PGA and α for the Wenchuan inventory is consistent with our modeling expectation that increasing PGA facilitates landslides over a greater range of length scales. This expectation is also reflected in the especially strong trend we resolve between PGA and the standard deviation in size for the Wenchuan inventory (Figure 10). However, while the relationship between landslide size and PGA may be statistically significant for very large datasets such as the Wenchuan inventory (N>10⁵), we argue that PGA alone is a secondary control on landslide size in general. As we have shown in the previous sections, topographic relief and hillslope material properties are also expected to alter landslide size statistics and their sensitivity to PGA, and we have not adjusted for these factors in the present analysis. Heterogeneity in these additional parameters may obscure the true relationship with PGA, especially if ground motions are concentrated in regions with anomalous relief or particularly strong/weak hillslope material properties. Indeed, the relatively larger differences in statistics between inventories compared to variations within a single dataset (Figure 10) suggest that landscape characteristics exert a stronger control on the distribution of landslide size compared to shaking intensity alone.

5 Discussion

5.1 Model Assumptions and Limitations

Our model results come with some important caveats. First, our method of discretizing hillslopes along hydraulic flow paths limits our landslide size predictions to be within the range of the finite distribution of measured slope segments. This limitation potentially censors landslides smaller than the smallest flow path (~grid cell size), and does not allow for smaller failures to form along a single flow path. A more comprehensive search for the most critical slope parcels is computationally challenging to implement at landscape scales and is beyond the scope of this study. However, we note that while our slope measurements do not include every conceivable landslide candidate patch, they do extend over much smaller length scales than our predicted landslides (Figure 6 and 7). Landslides are not predicted at these small scales because the assigned shear strength overwhelms the driving forces, not because of a paucity of small hillslopes. Thus we argue that our slope measurements do not significantly skew the landslide statistics in our simulations toward large sizes.

Second, we consider how our results depend on our choice of slope stability model. Clearly the rendering of all landslides as Culmann wedge-style failures is a crude approximation for shallow rock and soil slides, which are the most common failure mechanism in co-seismic inventories (Keefer, 1984). While the stability predicted by Culmann's analysis approaches that of the more-accurate log spiral mechanism for steep to vertical slopes, the difference is more pronounced as the slope flattens (Ling et al., 1999), meaning that our model under-predicts landslides on gentle slopes. Furthermore, Culmann's analysis is intended for slopes with a horizontal backfill which does not generally apply to our flow segment measurements, likely causing some over-prediction of failure plane length. While alternative limit equilibrium methods (e.g. ordinary method of slices, Spencer's method, etc.) provide a more accurate force balance, they require numerical techniques to discretize the sliding mass and identify the most critical failure plane. Thus the concessions in accuracy required by Culmann's analysis are another compromise for computational cost. Culmann's equation uniquely offers a closed form solution while preserving a 2D geometry and finite length scale, which are critical to our investigation of landslide scaling behavior. We also note that the mechanical and topographic controls on landslide size we observe in our simulations

agree with the results of previous authors (e.g., Katz and Aharonov, 2006; Klar et al., 2011; Frattini and Crosta, 2013; Milledge et al., 2014; Jeandet et al., 2019), suggesting that these factors are independent of the modelling approach.

5.2 Characteristic landslide distributions?

We view our key contributions to be the comparison of landslide statistics between different landscapes, and our emphasis on the mean landslide size rather than the power-law exponent. Regardless of whether the empirical data are truly lognormal, we show that landslide size distributions have a finite mean and variance that arise in our model due to the tradeoff between shear resistance and the availability of large hillslopes. While others have identified the same mechanical and topographic constraints before (e.g., Katz and Aharonov, 2006; Klar et al., 2011; Frattini and Crosta, 2013; Milledge et al., 2014; Jeandet et al., 2019), we are unaware of studies showing how these effects determine landslide size for landscapes with different properties. The correlations we found between relief, PGA, and mean landslide size in empirical data (Figures 9, 10) are broadly consistent with our model expectations, suggesting that landslide distributions carry the statistical fingerprints of the hillslopes and forcing event with which they are associated.

Our results lead us to propose the concept of characteristic landslide distributions. We suggest that large landslide events are associated with a characteristic landslide size, which represents the length scale at which relative shear resistance (i.e. the Factor of Safety) is minimized for the greatest portion of hillslopes in that region. Subsurface mechanical properties, seismic conditions, and the availability of hillslope relief set the landscape's potential for producing landslides of a given size. The combination of these factors creates optimal conditions for slope failure over a particular range of length scales, leading to the observed clustering of landslide sizes on a log histogram. We argue that the log-scale mean landslide size is thus 'characteristic' of the landscape and forcing event that caused the slopes failures.

Our theoretical framework differs from previous ideas about landslide scaling relations. In particular, the idea that landslide distributions cluster about a characteristic size contrasts with the scale invariance implied by the power law, inverse gamma, and double Pareto distributions, where the focus is nearly always on the slope of the heavy tail. The vast majority of landslides in each of the individual distributions shown in Figure 1 fall within two orders of magnitude in terms of area. This range might be considered large in practical terms, but we argue it is fairly small in the context of scale invariant phenomena (Evans, 2003). While we do not question the agreement with the power-law distribution for the largest landslides (e.g., Figure 2), we highlight that observed scaling relationships do not necessarily have a clear physical meaning (Clauset et al., 2009; Stumpf and Porter, 2012). Previous studies have reconciled divergence from power-law scaling by suggesting that landslides exhibit scale invariant behavior down to a threshold scale at the 'rollover', and that smaller length scales are associated with a distinct change in physics or observation bias (e.g. Malamud et al., 2004; Stark and Hovius, 2001; Katz and Aharonov, 2006; Stark and Guzzetti, 2009; Frattini and Crosta 2013; Tanyas et al., 2018). In contrast, we suggest that, compared to the range of length scales potentially available in natural landscapes, landslides are favored at relatively specific sizes.

6 Conclusion

Our simulations of landslide distributions demonstrate how landslide size is expected to vary on

average between landscapes with different properties. Consistent with the results of previous studies, we find the average landslide size reflects a trade-off between the cohesive strength of slope material and hillslope-scale relief. Our simulations also suggest that variations in PGA primarily change the variance in landslide size for earthquake triggered landslides, although the exact relationship depends on the specific hillslope characteristics of the landscape. Furthermore, we find correlations in empirical datasets that are broadly consistent with our model expectations. We argue that our focus on the finite mean and variance in landslide size rather than the power-law exponent allows us to resolve an empirical relationship with relief in particular. Finally, we propose the concept of characteristic landslide distributions, a conceptual framework which helps explain the empirical consistency between landslide frequency-size distributions and the lognormal statistical distribution.

Acknowledgments:

W.G.M. received support from a National Science Foundation (NSF) Graduate Research Fellowship. The work was also supported by NSF grants to M.K.C., D.Z., and A.J.W. (NSF-EAR 1640797 and 1640894). We thank David Milledge and one anonymous reviewer for scrupulous comments and suggestions that greatly improved the manuscript. We thank Kirk Townsend for technical assistance in developing our landslide model. We also thank Chris Massey's research group at GNS New Zealand for providing the polygon Kaikoura landslide inventory (v.1). The authors have no competing interests to declare.

References:

- Brardinoni, F., and Church, M. (2004). Representing the landslide magnitude-frequency relation: Capilano River basin, British Columbia. *Earth Surface Processes and Landforms*, 29(1), 115–124.
- Campbell, K., and Bozorgnia, Y. (2003) Updated near-source ground-motion (attenuation) relations for the horizontal and vertical components of peak ground acceleration and acceleration response spectra. *Bulletin of the Seismological Society of America*, 93(1), 314-331.
- Clauset, A., Rohilla Shalizi, C., & J Newman, M. E. (2009). Power-Law Distributions in Empirical Data. *SIAM Review*, *51*(4), 661–703.
- Clark, M.,K. and Zekkos, D. (2019). Characterization of landslides and rock mass strength leveraging the 2015 Mw 6.5 Lefkada Earthquake in Greece. Final Technical Report., U.S. Geol. Survey. National Earthquake Hazards Reduction Program, Award Number G17AP00088
- Crosta, G., Hermanns, R., Frattini, P., Valbuzzi, E., Valagussa, A. (2014). Large Slope Instabilities in Northern Chile: Inventory, Characterization, and Possible Triggers. *Landslide Science for a Safter Environment*, Springer International Publishing (2014), pp. 175-181.
- Culmann, C., (1875), Die Graphische Statik: Zurich, Switzerland, Meyer and Zeller, 644 p.

- Dreyfus, D., Rathje, E. M., & Jibson, R. W. (2013). The influence of different simplified sliding-block models and input parameters on regional predictions of seismic landslides triggered by the Northridge earthquake. *Engineering Geology*, 163, 41–54.
- Evans, I. S. (2003). Scale-specific landforms and aspects of the land surface. *Concepts and Modelling in Geomorphology: International Perspectives*, Terrapub, pp. 61–84.
- Fan, X., Scaringi, G., Korup, O., West, A. J., van Westen, C. J., Tanyas, H., Hovius, N., Hales, T.C., Jibson, R.W., Allstadt, K.E., Zhang, L., Evans, S.G., Xu, C., Li, G., Pei, X., Xu, Q., Huang, R. (2019). Earthquake-induced chains of geologic hazards: Patterns, mechanisms, and impacts. *Reviews of Geophysics*, *57*(2), 421-503
- Farr, T. G., Rosen, P. A., Caro, E., Crippen, R., Duren, R., Hensley, S., Kobrick, M., Paller, M., Rodriguez, E., Roth, L., Seal, D., Shaffer, S., Shimada, J., Umland, J., Werner, M., Oskin, M., Burbank, D., Alsdorf, D. (2007). The Shuttle Radar Topography Mission, *Reviews of Geophysics*, 45(2), 1–33.
- Frattini, P., Crosta, & G. B. (2013). The role of material properties and landscape morphology on landslide size distributions. *Earth and Planetary Science Letters*, *361*, 310–319.
- Gallen, S.F., Clark, M.K., Godt, J.W.(2015) Coseismic landslides reveal near-surface rock strength in a high-relief, tectonically active setting. *Geology*, 43(1), 11–14.
- Grieve, S. W. D., Mudd, S. M., & Hurst, M. D. (2016). How long is a hillslope? *Earth Surface Processes and Landforms*, 41(8), 1039–1054.
- Guzzetti, F., Malamud, B. D., Turcotte, D. L., & Reichenbach, P. (2002). Power-law correlations of landslide areas in central Italy. *Earth and Planetary Science Letters*, 195(3–4), 169–183.
- Harp, E. L., Hartzell, S. H., Jibson, R. W., Ramirez-Guzman, L., & Schmitt, R. G. (2014). Relation of landslides triggered by the Kiholo Bay Earthquake to modeled ground motion. *Bulletin of the Seismological Society of America*, 104(5), 2529–2540.
- Harp, Edwin L., and Jibson, Randall W., (1995) Inventory of landslides triggered by the 1994 Northridge, California earthquake: U.S. Geological Survey Open-File Report 95-213.
- Harp, E., Jibson, R., Schmitt, R., & Schmitt, R. G. (2016). Map of landslides triggered by the January 12, 2010, Haiti earthquake. US Geological Survey Scientific Investigations Map 3353, 15p., 1 sheet, scale 1:150 000
- Hovius, N., Stark, C. P., & Allen, P. A. (1997). Sediment flux from a mountain belt derived by landslide mapping. *Geology*, 25(3), 231–234.

- Hynes-Griffin, M. E., & Franklin, A. G. (1984). Rationalizing the Seismic Coefficient Method. U.S. Army Corps of Engineers Waterways Experiment Station. Miscellaneous Paper GL-84-13, 37pp
- Jeandet, L., Steer, P., Lague, D., Davy, P. (2019) Coulomb mechanics and relief constraints explain landslide size distribution. *Geophysical Research Letters*, 46, 4258-4266.
- Jibson, R. W. (2011). Methods for assessing the stability of slopes during earthquakes A retrospective. *Engineering Geology*, 122(1–2), 43–50.
- Katz, O., & Aharonov, E. (2006). Landslides in vibrating sand box: What controls types of slope failure and frequency magnitude relations? *Earth and Planetary Science Letters*, 247(3–4), 280–294.
- Keefer, D.K (1984) Landslides caused by earthquakes. GSA Bulletin, 95(4) 406-421
- Kelsey, K., Coghlan, M., Pitlick, J., & Best, D. (1995). Geomorphic analysis of streamside landslides in the Redwood Creek basin, northwestern California. US Geological Survey Professional Paper 1454, pp. J1-J12
- Klar, A., E. Aharonov, B. Kalderon-Asael, and O. Katz (2011), Analytical and observational relations between landslide volume and surface area. *Journal of Geophysical Research*, 116, F02001
- Legros, F. (2002). The mobility of long-runout landslides. *Engineering Geology*, 63(3–4), 301–331.
- Li, G., West, A. J., Densmore, A. L., Jin, Z., Parker, R., Hilton, G. (2014) Seismic mountain building: Landslides associated with the 2008 Wenchuan earthquake in the context of a generalized model for earthquake volume balance. *Geochemistry, Geophysics, Geosystems*, 15(4), 833-844
- Li, G., West, A. J., Densmore, A. L., Hammond, D. E., Jin, Z., Zhang, F., Wang, J., Hilton, R. G. (2016). Connectivity of earthquake-triggered landslides with the fluvial network: Implications for landslide sediment transport after the 2008 Wenchuan earthquake, *Journal of Geophysical Research: Earth Surface*, *121*(4), 703-724
- Ling, H. I., Mohri, Y., & Kawabata, T. (1999). Seismic analysis of sliding wedge: extended Francais Culmann's analysis. *Soil Dynamics and Earthquake Engineering*, 18(5), 387–393.
- Liucci, L., Melelli, L., Suteanu, C., & Ponziani, F. (2017). The role of topography in the scaling distribution of landslide areas: A cellular automata modeling approach. *Geomorphology*, 290, 236–249.

- Malamud, B. D., Turcotte, D. L., Guzzetti, F., & Reichenbach, P. (2004). Landslides, earthquakes, and erosion. *Earth and Planetary Science Letters*, 229(1–2), 45–59.
- Massey, C., Townsend, D., Rathje, E., Allstadt, K. E., Lukovic, B., Kaneko, Y., Bradley, B., Wartman, J., Jibson, R.W., Petley, D.N., Horspool, N., Hamling, I., Carey, J., Cox, S., Davidson, J., Dellow, S., Godt, J.W., Holden, C., Jones, K., Kaiser, A., Little, M., Lyndsell, B., McColl, S., Morgenstern, R., Rengers, F.K., Rhoades, D., Rosser, B., Strong, D., Singeisen, C., Villeneuve, M. (2018). Landslides Triggered by the 14 November 2016 Mw7.8 Kaikōura Earthquake, New Zealand. *Bulletin of the Seismological Society of America*, 108(3), 1630–1648.
- Milledge, D.G., Bellugi, D., McKean, J.A., Densmore, A.L., Dietrich, W.E. (2014). A multidimensional stability model for predicting shallow landslide size and shape across landscapes. *Journal of Geophysical Research: Earth Surface*, 119(11), 2481-2504
- Montgomery, D.R., & Foufoula-Georgiou, E. (1993) Channel network source representation using digital elevation models. *Water Resources Research*, 29(12), 3925-3934
- O'Callaghan, J.F., and Mark, D.M. (1984) The Extraction of Drainage Networks from Digital Elevation Data. *Computer Vision, Graphics, and Image Processing, 28*(3), 332-344.
- OCM Partners, 2018: 2004 Coastal California IfSAR: Digital Elevation Model (DEM) from 2010-06-15 to 2010-08-15. NOAA National Centers for Environmental Information, https://inport.nmfs.noaa.gov/inport/item/49440
- Pelletier, J. D., Malamud, B. D., Blodgett, T., & Turcotte, D. L. (1997). Scale-invariance of soil moisture variability and its implications for the frequency-size distribution of landslides. *Engineering Geology*, 48(3–4), 255–268.
- Roback, K., Clark, M., West, J., Zekkos, D., Li, G., Gallen, Sean., Chamlagain, D., Godt, J. (2018). The size, distribution, and mobility of landslides caused by the 2015 Mw7.8 Gorkha earthquake, Nepal. *Geomorphology*, 301, 121-138
- Schmidt, K. M., & Montgomery, D. R. (1995). Limits to Relief. *Science*, 270(5236), 617–620.
- Stark, C. P., & Guzzetti, F. (2009). Landslide rupture and the probability distribution of mobilized debris volumes. *Journal of Geophysical Research: Earth Surface*, 114(2), 1–16.
- Stark, C., & Hovius, N. (2001). The characterization of landslide size distributions. *Geophysical Research Letters*, 28(6), 1091–1094.

- Stumpf, M. P. H., & Porter, M. (2012). Critical Truths About Power Laws. *Science*, *335*(6069), 665–666.
- Tanyaş, H., van Westen, C. J., Allstadt, K. E., Nowicki Jessee, M. A., Görüm, T., Jibson, R. W., Godt, J., Sato, H.P., Schmitt, R.G., Marc, O., Hovius, N. (2017). Presentation and Analysis of a Worldwide Database of Earthquake-Induced Landslide Inventories. *Journal of Geophysical Research: Earth Surface*, *122*(10), 1991-2015.
- Tanyaş, H., van Westen, C. J., Allstadt, K. E., Jibson, R. W. (2018). Factors controlling landslide frequency-area distributions. *Earth Surface Process and Landforms*, 44, 900-917.
- ten Brink, U. S., Geist, E. L., & Andrews, B. D. (2006). Size distribution of submarine landslides and its implication to tsunami hazard in Puerto Rico. *Geophysical Research Letters*, *33*(11), 23–26.
- Townsend, K., Gallen, S., & Clark, M. (in review 2019). Co-evolution of rock strength and relief during the early stages of mountain building. *In review Journal of Geophysical Research: Earth Surface*.
- Valagussa, A., Marc, O., Frattini, P., & Crosta, G. B. (2019). Seismic and geological controls on earthquake-induced landslide size. *Earth and Planetary Science Letters*, 506(15), 268–281.
- Wartman, J., Dunham, L., Tiwari, B., & Pradel, D. (2013). Landslides in eastern Honshu induced by the 2011 Off the Pacific Coast of Tohoku earthquake. *Bulletin of the Seismological Society of America*, 103(2B), 1503–1521.
- Whipple, K. X., & Tucker, G. E. (1999). Dynamics of the stream-power river incision model: Implications for height limits of mountain ranges, landscape response timescales, and research needs. *Journal of Geophysical Research*, 104(B8), 17661.
- Xu, C., Xu, X., Yao, X., & Dai, F. (2014). Three (nearly) complete inventories of landslides triggered by the May 12, 2008 Wenchuan Mw 7.9 earthquake of China and their spatial distribution statistical analysis. *Landslides*, 11(3), 441–461.
- Zekkos, D., Clark, M., Cowell, K., Medwedeff, W., Manousakis, J., Saroglou, H., & Tsiambaos, G. (2017). Satellite and UAV-enabled mapping of landslides caused by the November 17th 2015 Mw L6.5 Lefkada earthquake. *Proceedings of the 19th International Conference on Soil Mechanics and Geotechnical Engineering, Seoul* 2017, 2235–2238.